Solid State Sciences 139 (2023) 107171

Contents lists available at ScienceDirect

Solid State Sciences

journal homepage: www.elsevier.com/locate/ssscie

Tailored $CuCl_2$ nanoparticles for glutamine and ammonia biochemical sensing applications

Anesu Nyabadza[a,b,c,*], Éanna McCarthy[a,c], Karsten Fleischer[a,c], Sithara Sreenilayam[a,c], Ahmed Al-Hamaoy[c,d], Mercedes Vazquez[a,b,c], Dermot Brabazon[a,b,c]

[a] I-Form Advanced Manufacturing Centre Research, Dublin City University, Glasnevin, Dublin, 9, Ireland
[b] EPSRC & SFI Centre for Doctoral Training (CDT) in Advanced Metallic Systems, School of Mechanical & Manufacturing Engineering, And School of Chemical Sciences, Dublin City University, Glasnevin, Dublin, 9, Ireland
[c] Advanced Processing Technology Research Centre, Dublin City University, Glasnevin, Dublin, 9, Ireland
[d] College of Engineering, Al-Nahrain University, Baghdad, Iraq

ARTICLE INFO

Keywords:
Plasmon sensor
Conductive inks
Biochemical sensing
Laser ablation
Copper nanoparticles

ABSTRACT

In this study, CuCl2 nanoparticles (NPs) synthesised via pulsed laser ablation in liquid (PLAL) were successfully employed to simultaneously detect glutamine and ammonia, with a limit of detection of 20 nM and up to 1500 ppm, respectively. These NPs hold potential for non-invasive diagnosis and monitoring of various health conditions using urine and sweat samples. The sensing mechanism relied on the plasmon peaks of $CuCl_2$ NPs in the UV range (at 300, 363, and 423 nm), which were used to correlate the levels of glutamine and ammonia concentration with the absorbance. Quasi-spherical CuO and pyramidal $CuCl_2$ NPs were synthesised through laser ablation of Cu powder in liquid IPA and IPA-HCl, respectively. $CuCl_2$ NPs displayed higher ablation efficiency, higher optical absorbance (20-fold), and an 8400-fold increase in colloidal conductivity (0.0005 vs 4.2 mS/cm) compared to CuO NPs. The NP size distribution ranged broadly from 10 nm to less than 100 nm. XPS analysis revealed that ablation in pure IPA resulted in oxidized Cu NPs, while ablation in IPA-HCl liquid medium (12 nM HCl) led to the formation of a combination of metallic copper and $CuCl_2$ NPs that were more conductive and had higher optical absorbance than their oxidized counterparts.

1. Introduction

The detection of low concentrations of biological molecules is an emerging and innovative application of nanoparticles (NPs) [1–3]. Plasmon sensors based on NPs enable non-invasive, low-cost, sustainable and rapid health diagnosis and monitoring methods [4]. Glutamine, one of the 20 canonical amino acids and the most abundant one, gives the best example of the versatility of amino acid metabolism and diverse physiological functionality, including an important role in immune function [5,6]. Glutamine is detectable in urine, sweat and saliva, which enables for non-invasive mechanisms of detection. Glutamine is an important energy and nitrogen source in human cells. Furthermore, glutamine creates 60% of the total amino acids within muscles and 20% of the total amino acids in the human body. Humans consume 3–6 g of glutamine daily through food, and some atheletes consume 20–30 g of gutamine daily via a combination of supplementation and food [7]. Glutamine metabolism rate is similar or higher to that of glucose and certain concentrations (in the nM-mM range) are closely linked to diseases involving ammonia imbalance such as ammonia intoxication, hyperammonemias and protein intolerance [2]. Glutamate is also an excitatory neurotransmitter in the central nervous system. High concentration of glutamate is linked to many neurologic disorders hence; there is a need for highly accurate, selective, and repeatable glutamate detection technologies. It has been recorded that glutamine levels increased in the cerebrospinal fluid during hepatic coma and Reye's syndrome in children [2]. During cancer treatment, tumour cells can be starved of glutamine to inhibit their growth [8]. In one report, it was observed that cancer cells are addicted to glutamine, which opened a method to kill these by starving them of glutamine [9]. The sensing of glutamine is therefore an important tool to indicate the state of human health.

Nanoparticle-based sensors have gained attention in biochemical sensing owing to their advanced physicochemical properties such as UV light absorbance [1,10–12], fluorescent properties, high reactivity, high

* Corresponding author.
E-mail address: anesu.nyabadza3@mail.dcu.ie (A. Nyabadza).

https://doi.org/10.1016/j.solidstatesciences.2023.107171
Received 26 January 2023; Received in revised form 9 March 2023; Accepted 27 March 2023
Available online 28 March 2023
1293-2558/

sensitivity (for sensing very small concentrations e.g., in the nM range), high surface area-to-volume ratio and plasmon effects [11–16]. The use of NP plasmon properties coupled with UV–Vis measurements provides a low-cost, cheap and highly accurate mechanism of sensing [14,17,18]. Either a shift of the plasmon peak or a change in its absorbance (intensity) with increasing analyte concentration is used as a sensing mechanism. Many diseases including Parkinson's disease, diabetes and Alzheimer's are linked to a high release of H_2O_2 [14]. Jiang et al. [14] used Ag–Au bimetallic NPs as H_2O_2 detectors by correlating the UV–Vis absorbance values at the 426 nm plasmon peak with the H_2O_2 concentration ranging from 16 μM to 1 mM. The UV–Vis absorbance increased non-linearly with increasing H_2O_2 concentration. Another research team used Au–MnO bimetallic NPs for the detection of H_2O_2 [19]. The aforementioned study recorded an incredibly low detection limit of 8 nM, which is much lower than the previously mentioned study by Jiang et al. [14], thereby demonstrating the dependency of biochemical sensitivity on the sensing material properties. Moreover, Albayrak et al. [2] used ZnO nanorods for the detection of glutamine. The concentration of glutamine was correlated to the colloidal potential difference (mV). Similarly, Zeynaloo et al. [13] used Ag NPs to detect glutamine concentrations via amperometric and voltammetric measurements. The detection of molecules in urine and sweat enables non-invasive diagnosis and monitoring. Glutamine plasmon sensors must be able to detect glutamine in the presence of other molecules such as ammonia. Ammonia concentrations in urine and sweat are also indicative of several health conditions including kidney failure, diabetes, hepatic disease and hyperammonemia [20–24].

Cu NPs have gained research attention for their application in plasmon sensors owing to their surface plasmon resonance, photoluminescence and bandgap energy [25–29]. Other metals such as Au NPs and Ag NPs are also used in plasmonic and electrical applications however, these are much more expensive and less sustainable than Cu [27,28,30–32]. Therefore, Cu NPs have become a major replacement candidate for these other metals. A major research challenge during the synthesis is that Cu colloids are prone to oxidation and sedimentation, which inhibits their light absorption efficiency, reactivity and conductivity. Hence, more research and innovation on non-oxidising and non-sedimenting techniques are required to advance the field of plasmon sensors [25–28].

The use of Pulsed Laser Ablation in Liquid (PLAL) has gained popularity for creating new nanomaterials with various applications, such as sensing, medical and catalysis [6,33–37]. PLAL involves a laser that ablates a target material submerged in liquid, causing local vaporization and bond breaking [15,35,38,39]. This creates plasma plumes that form cavitation bubbles, within which various reactions occur, including atom attachment, nucleation, growth, and NP formation. The cavitation bubble eventually collapses or explodes due to pressure differences between the inside and outside of the bubble, ejecting particles into the liquid medium. The ejected NPs stay small due to quick cooling within the liquid medium, but they may still grow during ablation if enough Gibbs free energy is supplied (e.g., from secondary photon absorption), or through local melting that induces particle attachment. Agglomeration events can also lead to particle growth after formation. The liquid medium is heavily involved during the PLAL process, atoms from the liquid medium are also vaporised during the process and are available for bonding during NP formation [40–42]. For example, PLAL in organic liquids often leads to the formation of carbides or NPs with a carbon coating. Recently, Shreyanka et al. [33] synthesised transition-metal-based 3D metal–organic framework (MOF) using PLAL. Various *N*P-based MOFs were synthesised via the same laser system including Cu, Co and Ni.

Herein, PLAL was used to fabricate CuO, metalc Cu, and $CuCl_2$ NPs via PLAL of Cu powders under liquid IPA and IPA-HCl respectively. The shape of the synthesised NPs varied depending on the liquid medium used for the synthesis process. Specifically, IPA resulted in the production of spherical and quasi-spherical NPs, while IPA-HCl led to the formation of pyramidal NPs. Broad NP size distributions were observed, including both small particles (<10 nm) and larger particles (>100 nm). XPS and EDX analysis were employed to investigate the chemical composition of the NPs, and UV–Vis and FTIR techniques were used to examine their optical properties. The high optical absorbance of $CuCl_2$ NPs allowed for their successful application in sensing ammonia and glutamine. The plasmon property of $CuCl_2$ NPs was used as a mechanism to detect ammonia and glutamine, with a detection range of 20–1500 nM. In particular, the detection limit for glutamine sensing was determined to be 20 nM.

2. Materials and methods

Laser ablation experiments were conducted by a Nd:YAG laser system (WEDGE HF 1064, Bright Solutions) with pulses centred at 1064 nm. The laser was set to a pulse width of 600 ps, a repetition rate of 10 kHz, a scan speed of 3.5 m/s and an ablation time of 20 min. The laser scanned in an Archimedean spiral pattern with 50 μm hatch spacing and 55 mm outer diameter. PLAL experiments were conducted in Batch mode and three repeat experiments were done for each condition (n = 3). 4.5 g of copper powder (Sigma Aldrich, Ireland Limited, spheroidal powder, 10–25 μm, 98% purity) was placed at the bottom of 12.5 ml of each liquid media held in a glass beaker (60 mm inner diameter) for each PLAL experiment. This ensured a liquid layer height of 5 mm above the target powder. Pure IPA and IPA with HCl (6 and 12 mM) were used as liquid media. Pure IPA, IPA-HCl 6 mM and IPA-HCl 12 mM liquids had pH values of 6.9, 1.9 and 1.7 respectively; pH reading were conducted using the Hanna Instruments pH meter, model number pH 210, with temperature compensation. DI water, ethanol and toluene were also explored but these were deemed incompatible with Cu powder ablation without powder compaction due to server NP sedimentation. The results with these solvents are included for completeness in the supplementary information section. A schematic of the PLAL process is shown in Fig. 1.

Five concentrations of glutamine amino acid (100 ml - L-Glutamine, BioSciences Limited, Ireland, 200 mM) were added to diluted colloids for glutamine detection experiments. The IPA-HCl colloids of $CuCl_2$ NPs (12 mM HCl concentration) were used for detection studies. A volume of 0.5 μl of $CuCl_2$ colloid was diluted by 2 ml of IPA and various volumes of glutamine were added. The volumes were 0.2, 0.4, 1, 5, 7, 11, 15 and 20 μl and these produced glutamine concentrations of 20, 40, 100, 500, 700, 1100 and 1500 nM respectively. The mixtures were shaken by hand for 2 s and analysed immediately via UV–Vis. Three repeat measurements were conducted per mixture (n = 3) and 95% confidence intervals were established. A volume of 1 μl of $CuCl_2$ colloid was diluted in 2 ml IPA and used for the detection of ammonia/ammonium ions. Various concentrations of ammonium buffer solution (Ammonium Chloride/ammonia, pH 10–11, Sigma Aldrich, Ireland limited) were added to the diluted colloid and shaken for 2 s before UV–Vis measurements (n = 3). Various volumes of ammonia were added to the colloid for detection in the range of 0.5–3 μl which provided ammonia concentrations between

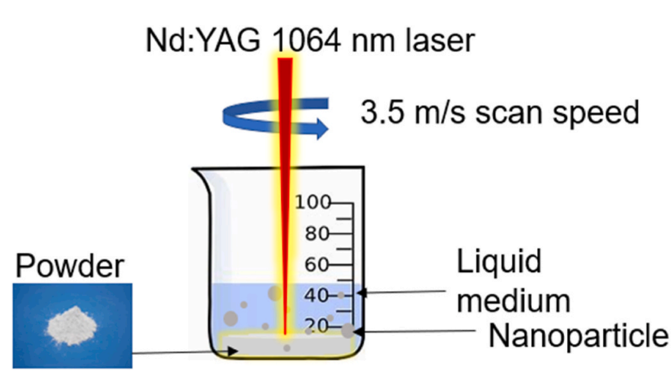

Fig. 1. A schematic of the Pulsed laser ablation in liquid process.

250–1500 ppm. The detection of glutamine concentrations of 100, 200 and 300 nM within colloids containing 500 and 1500 ppm of ammonia were investigated.

Ultraviolet–visible spectroscopy (UV–Vis) was recorded in a quartz cuvette (10 mm pathlength, Helma) with Varian Cary 50 UV–Vis spectrophotometer after each PLAL experiment. A scan range of 190–900 nm with a scan rate of 200 nm/min was used. All the optical spectra were corrected for the liquid media absorption by subtracting the contribution of the liquid medium from the recorded spectrum. Each sample was diluted by its liquid media before analysis to avoid signal saturation, dilution factors of 5 (IPA, DI water, ethanol and toluene samples) and 96 (IPA + HCl samples) were used. A dilution factor of 5 means that; 4 parts dilution liquid and 1 part colloid were mixed.

Fourier-Transform Infrared Spectroscopy (FTIR) measurements were recorded for the dried Cu NPs. A volume of 0.1 ml of IPA-synthesised colloids was deposited using a pipette and left for 1 min to dry onto the FTIR crystal for analysis. The scan range was set to 4000 - 400 cm^{-1}; four repeat measurements were collected and averaged by the instrument.

Field emission scanning electron microscopy (FESEM) (FESEM-Hitachi S5500 Field Emission SEM) imaging was conducted on the dried Cu NPs on circular copper grids. The sample preparation for FESEM involved micro-pipetting a volume of 0.2 μl onto a copper grid with the assistance of a light microscope to ensure accurate deposition.

Energy dispersive x-ray analysis (EDX) was used to study the chemical composition of the Cu NPs. The Cu NP size distribution, mean NP size, concentration (particles per ml), zeta potentials and colloidal conductivity were measured via dynamic light scattering (DLS) (Malvern Zetasizer Ultra, Malvern Instruments Ltd)). Eight measurements were taken for each sample and averaged.

For X-ray photoelectron spectroscopy (XPS) characterisation, the colloids were drop cast onto a conductive carbon adhesive substrate, to ensure a conductive path, and allowed to dry in air. The characterisation was carried out in a UHV Omicron system with a DAR 400 twin-anode x-ray source and EA 125 energy analyzer. All samples were Ar + ion sputtered using a Prevac IS40C1 ion gun at 5×10^{-6} mbar of argon, 0.65 kV, and 5 mA emission current for 15 min before characterisation, to clean the surface layer which may inhibit signal from the deposited material, particularly at low kinetic energy.

Viscosity measurements for conductive ink applications were conducted on a Brookfield DVNext Cone/Plate Viscometer. Glycerol (99.5% purity, Sigma Aldrich, Ireland Limited) was used to increase viscosity. Viscosity was measured over a 1 min period (1000 readings) and an average value was reordered.

3. Results

3.1. Morphology and chemical composition

FESEM analysis recorded that quasi-spherical Cu NPs were synthesised in IPA as shown in Fig. 2 a-b. Two groups involving small and large NPs were recorded; thus bimodal size distributions exist. The aggregation of small Cu NPs is confirmed in Fig ab whereby a group of small Cu NPs about 5–20 nm in diameter are aggregated together to form porous monolithic structures. This agrees with the colloidal visual inspection where IPA-synthesised colloids exhibited some level of sedimentation. Conversely, pyramidal Cu NPs were formed in IPA-HCl liquid medium (both the 12 and 6 mM HCl concentrations) as shown in Fig. 2 c-d. The NP size distribution was calculated via image processing in MATLAB (2022 version) of FESEM images. The image processing algorithm can be found in the supplementary information section. Fig. 2 a and d were used during image processing and the resulting NP size distrubutions are shown in Fig. 2 e and f respectively. Additionally, MATLAB was used to calculate statistical data from the FESEM images. The mean, standard deviation from the mean (SD), meadian and mode NP diameter from Fig. 2a were 226, 179, 117 and 307 nm respectively. The mean, SD, meadian and mode NP diameter size from Fig. 2d were 43, 31, 37 and 56 respectively. The mean NP diameters were also measured by DLS, which accounts for every particle within the measurement vial. This differs form image processing whereby a small proportion of the NPs (particles within the image) is analysed. However, image processing of FESEM images has its merits including the ability to distinguish shapes and to separate agglomerated or attached particles via by modifying the filters within the image processing code. FESEM can also account for very small partcles (e.g., <1 nm), which the DLS might miss especially in the presence of large particles.

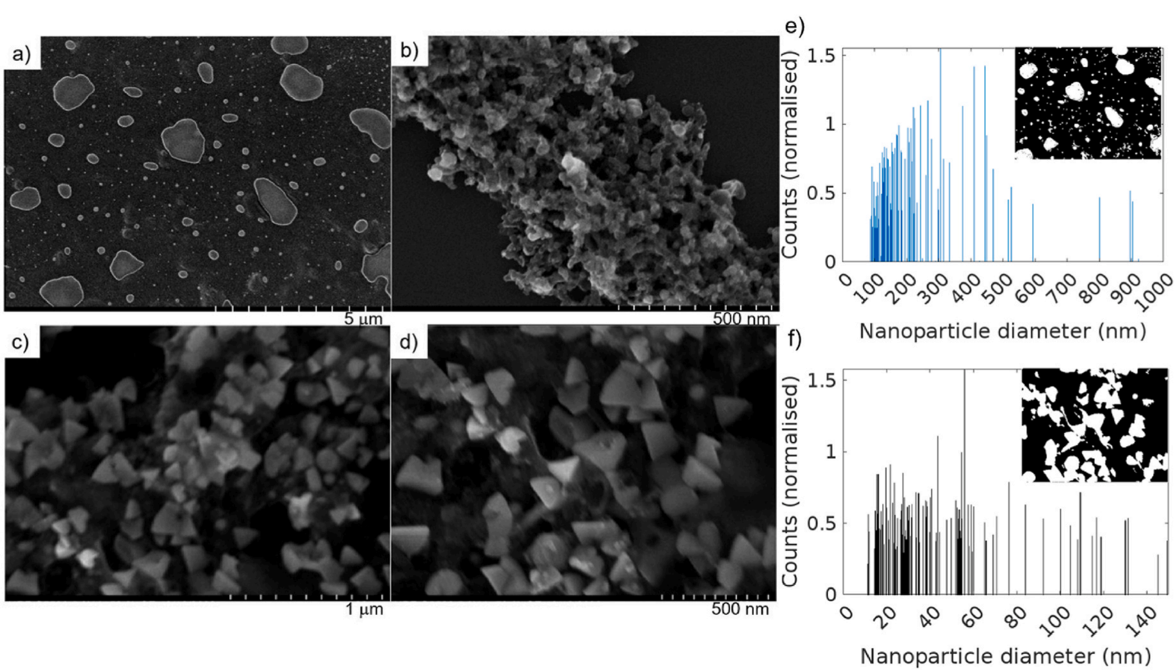

Fig. 2. Field emission scanning electron microscopy of; a-b) CuO nanoparticles synthesised in IPA; c-d) $CuCl_2$ nanoparticles synthesised in IPA-HCl; e) nanoparticle size distribution of CuO nanoparticles generated from image processing and; f) nanoparticle size distribution of $CuCl_2$ nanoparticles generated from image processing.

The chemical composition of the colloids was analysed via EDX, XPS and UV–Vis. EDX mapping reviewed that CuO NPs were formed when pure IPA was used as a liquid medium while $CuCl_2$ NPs were formed when IPA-HCl liquid medium was used (both the 12 and 6 mM HCl concentrations). The analysed EDX region for an IPA-synthesised sample is shown in Fig. 3a and the corresponding chemical composition mapping is shown in Fig. 3 b-c. The analysed EDX region for an IPA-HCl-synthesised sample (6 mM HCl) is shown in Fig. 3d and the corresponding chemical composition mapping is shown in Fig. 3 e-f. The chemical composition in weight percentages are as follows; Cu NPs in IPA: copper = 72%, oxygen = 27%, chlorine = 0%, Cu NPs in IPA-HCl (6 mM HCl): copper = 67%, oxygen = 2%, chlorine = 31%, Cu NPs in IPA-HCl (12 mM HCl): copper = 65%, oxygen = 1%, chlorine = 34%.

The Cu 2p 3/2 peaks for the IPA and IPA-HCl samples are presented in Fig. 4a. Deconvolved components were fit using Gaussian-Lorentzian functions, with fixed FWHM to limit the number of free parameters. Additional components were only included when they reduced the RMS of the fit. The Cu 2p 3/2 peaks appear to be composed of one to three components. The pure IPA sample shows a single component with peak position of 933.9 eV. This indicates that the material is highly oxidized as CuO, with any metallic Cu or Cu_2O being below the limits of detection. The sample with IPA with 6 mM of HCl shows three components at 931.35, 933.4, and 935.4 eV. The lowest binding energy component can be attributed to metallic Cu or Cu_2O, as the position for these are too close to be distinguished [43]. The middle component can be attributed to CuO, and the higher binding energy component may be due to $CuCl_2$. The percentage concentration of these components is 17, 59, and 24%, for Cu/Cu_2O, CuO, and $CuCl_2$, respectively. The sample with IPA with 12 mM of HCl also shows three components, with similar positions (931.9, 933.1, and 934.6 eV). The balance of components is shifted compared to the lower HCl sample, with a notable shift towards Cu/Cu_2O in this sample. The percentage concentration for this sample is 54, 30, and 16%, for Cu/Cu_2O, CuO, and $CuCl_2$, respectively. These results suggest that increasing concentration of HCl may promote the formation of metallic copper nanoparticles, however the close energetic position of metallic Cu and Cu_2O makes a definite assignment to metallic Cu difficult.

The O 1s peaks for the IPA and IPA-HCl samples are presented in Fig. 4b. Deconvolved components were fit using Gaussian-Lorentzian functions, again with fixed FWHM to limit the number of free parameters and additional components only being included when they reduced the RMS. The O 1s peaks appear to be composed of one to two components. The component at lower binding energy is consistent with the presence of metal oxides (CuO or Cu_2O) in the sample. The samples show this low binding energy component diminishing with increasing HCl concentration, to being below the limit of detection for the IPA +12 mM HCl sample. This strongly supports the Cu 2p results in suggesting there is an increasing amount of metallic Cu and $CuCl_2$ with increasing concentration of HCl (and thus less oxide, or no oxide for the higher HCl concentrations).

3.2. Optical properties

UV–Vis and FTIR were used to examine the optical properties of the colloids. The IPA-synthesised samples exhibited two plasmon peaks; one at 305 and another one at 600 nm with a lower absorbance as shown in Fig. 5a (UV–Vis analysis). On the other hand, the IPA-HCl-synthesised samples exhibited three plasmon peaks; one peak at 300 nm, a second peak at 363 nm with a lower absorbance and a third peak at 423 nm with the lowest absorbance among the three. These peaks could be attributed to the different version of Cu within the colloid including $CuCl_2$, Cu_2O and metallic copper as reviewed by the XPS analysis. Recall that a dilution factor of 5 (4 parts dilution liquid and 1 part colloid) was used during analysis for IPA samples while a much higher dilution factor of 96 was used for IPA-HCl samples due to a much higher absorbance for these samples. A higher absorbance is attributed to a higher NP yield, a higher optical absorbance property, or a combination of both. The as-fabricated CuO colloids in IPA exhibited a dark brown colour while the $CuCl_2$ colloids in IPA-HCl exhibited a yellow-green colour as shown in Fig. 5c. Moreover, other liquids were also explored including ethanol, DI water and toluene and these exhibited a single plasmon peak (around 300 nm). DI water and ethanol displayed similar maximum absorbance values to IPA (<0.6 a. u). The toluene samples exhibited higher maximum absorbance of 2.5 a. u., a value that is still much lower than the IPA-HCl samples (factoring in the dilution factors of 5 vs 96), more details about the DI water, ethanol and toluene samples are found in the supplementary information section.

The FTIR spectrum of dried CuO NPs that were fabricated in IPA is shown in Fig. 5d. The spectrum was generated by drop casting 0.1 ml of the *as*-synthesised colloid onto the FTIR crystal and leaving it for 1 min

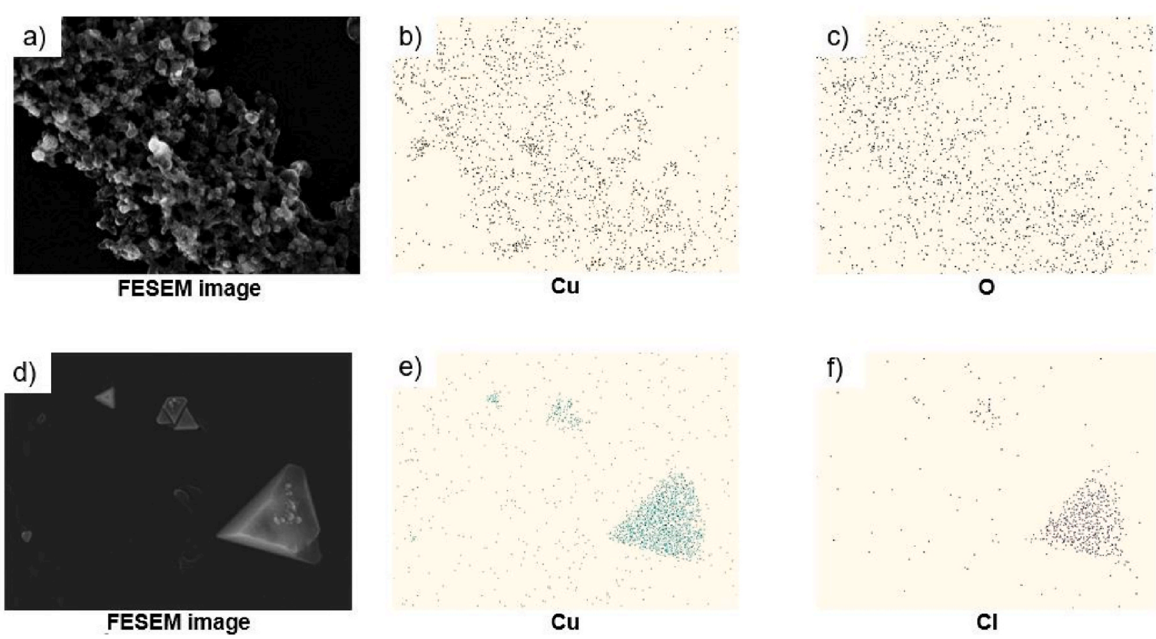

Fig. 3. Energy Dispersive X-Ray analysis and mapping of a-c) CuO nanoparticles synthesised in IPA; and d-f) $CuCl_2$ nanoparticles fabricated in IPA-HCl.

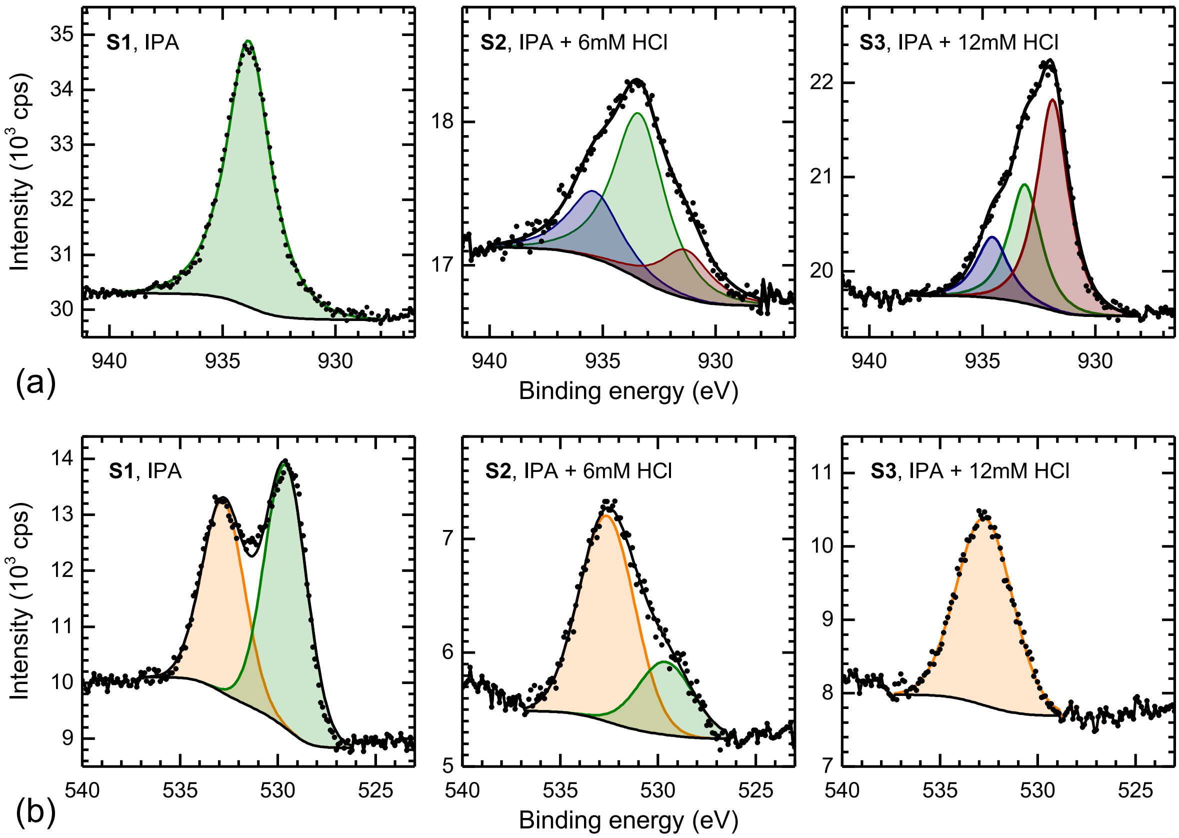

Fig. 4. (A) XPS results showing the copper Cu 2p 3/2 peak for the IPA and IPA-HCl samples, with components fit for metallic Cu/Cu2O (red), CuO (green), and CuCl2 (blue); (b) XPS of the oxygen O 1s peak for the same samples. Components fit residual hydroxides (orange) and metal oxides (green).

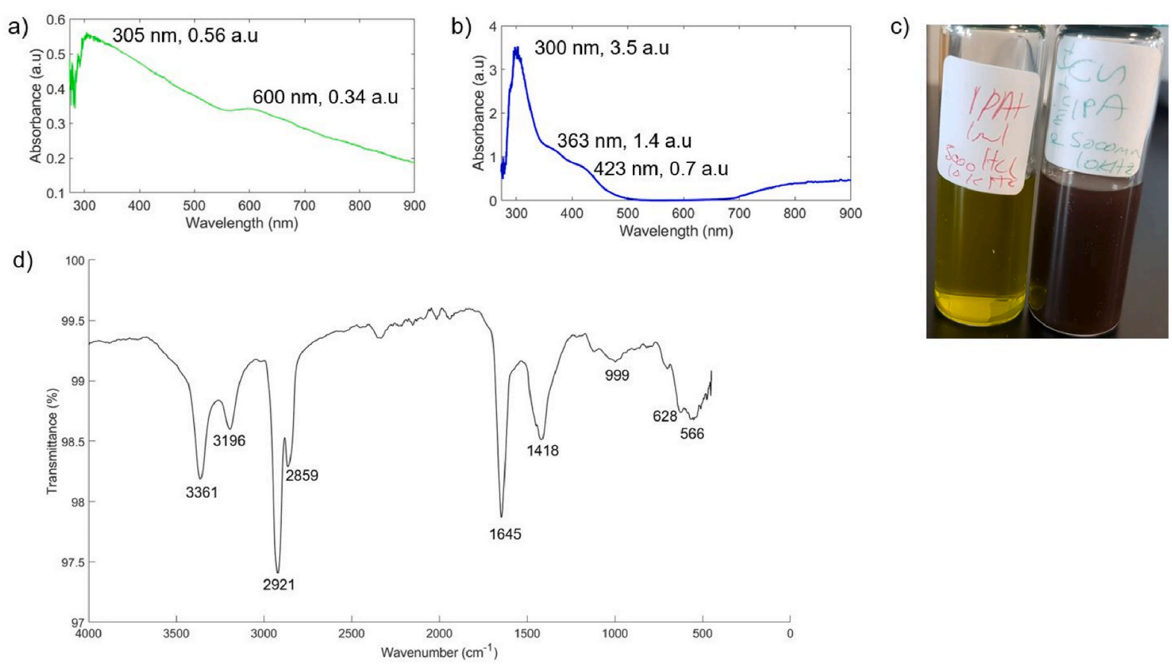

Fig. 5. Ultraviolet–visible spectroscopy analysis of a) CuO nanoparticles synthesised in IPA; and b) $CuCl_2$ nanoparticles fabricated in IPA-HCl; c) $CuCl_2$ (left) and CuO (right) colloids; and d) Fourier-transform infrared spectroscopy analysis of CuO nanoparticles.

to dry. IPA dry's in the air quickly, which is one of its advantages in PLAL, especially during characterisation (FTIR, SEM, XPS and others) and inkjet printing applications.

3.3. *Detection of L-Glutamine amino acid and ammonia using Cu NP plasmon properties*

Various concentrations of glutamine were mixed with diluted $CuCl_2$

colloids that were synthesised in IPA-HCl liquid (12 mM HCl concentration). The mixtures were shaken by hand for 2 s and immediately analysed by UV–Vis. This demonstrates the fast response time of the detection method. Changes in $CuCl_2$ NP absorbance (intensity) at the plasmonic peak (300 nm) were used as an indicator for the detection of glutamine concentrations. The UV–Vis absorbance increased with increasing glutamine concentration as shown in Fig. 6a. The UV–Vis absorbance started to respond with statistical significance at a glutamine concentration of 20 nm, which is the limit of detection. Fig. 6b shows a monotonically increasing relationship between the glutamine concentration and the absorbance.

The $CuCl_2$ NPs also detected ammonia/ammonium ions. The concentration of ammonium was correlated to the UV–Vis absorbance as shown in Fig. 7a. The UV–Vis absorbance at 300 nm decreased in a logarithmic manner with increasing ammonium concentrations between 0 and 500 ppm. A red shift in the UV–Vis spectra from 300 to 341 nm was recorded for ammonium concentrations greater than 750 ppm. Additionally, an immediate colour change from yellow-green to milky-white was observed for ammonium concentrations greater than 750 ppm. The absorbance at 341 nm decreased linearly with increasing ammonium concentration from 750 ppm as shown in Fig. 7c.

The $CuCl_2$ plasmon sensor can also detect glutamine in the presence of ammonia. Fig. 7d shows the effect of increasing the glutamine concentration in the presence of 500 ppm ammonium. The glutamine concentration is inversely proportional to the absorbance at 300 nm in the presence of 500 ppm ammonium. A similar result was recorded for an ammonium concentration of 1500 ppm as shown in Fig. 7e. From Fig. 7 d and e it can be seen that an increase in ammonium concentration made the sensor more sensitive to changes in glutamine concentrations (between 100 and 300 nM).

3.4. *Colloidal stability, concentration, size, electrical properties and viscosity*

Colloidal stability was assessed both qualitatively and quantitatively. Qualitative analysis was done by visual inspection whereby, visible agglomeration or NP sedimentation or both evidenced colloidal instability. Colloids that were synthesised in DI water, ethanol and toluene displayed high levels of NP instability, which was evidenced by NP agglomeration and settling at the bottom (sedimentation) immediately after PLAL experiments (see supplementary information section for colloid images). Various laser processing parameters were explored in pursuit to alleviate the sedimentation but to no avail (see the supplementary section for these experiments). IPA liquid showed lower visible agglomeration than ethanol, DI water and toluene samples, while IPA-HCl samples displayed no agglomeration and no sedimentation. Colloidal stability was also measured quantitatively via DLS by measuring the Zeta potentials. The Zeta potential values are shown in Table 1. The IPA-HCl liquid media is deemed the most suitable for achieving colloidal stability than any of the other media herein, and pure IPA came second best. The NP size and concentration (in particles/ml) were measured via DLS. The relative ablation efficiency among the samples was calculated according to Equation (1) and the results are shown in Table 1. The colloidal conductivities (mS/cm) were measured via DLS for conductive inks applications and the results are shown in Table 1. The IPA-HCl liquid compared to pure IPA increased the ablation efficiency by a maximum of 50-fold, reduced the NP mean size from 120 to 53 nm, increased the NP stability (no sedimentation and higher Zeta potentials) and achieved an 8400-fold increase in electrical conductivity from 0.005 to 4.2 mS/cm.

$$E = \mu c / m \quad (1)$$

where E is the relative ablation efficiency, μ is the mean NP diameter (nm), c is the NP concentration (particles/ml) and m is the highest NP concentration multiplied by the NP mean size from Table 1 ($20.2 \times 86 = 1737.2$).

The viscosity of colloids increased with increasing NP concentration and size (ablated mass) as shown in Table 1.

4. Discussion

4.1. *Conductive ink application*

Colloidal sedimentation is caused by a combination of weak van der Waals forces of attraction, weak particle charges (low Zeta potentials) and the high density of the Cu NPs. HCl in two different concentrations (6 and 12 mM) was added to IPA before the PLAL process to produce an IPA-HCl hybrid liquid. This introduced some surface charges on the Cu NPs that cause forces of repulsion among them. Additionally, HCl is a reducing agent, which reduces the Cu NPs thereby alleviating them from the typical oxide layers on the surfaces. This induces NP surface charges thereby inhibiting aggregation. This resulted in stable $CuCl_2$ NPs. The HCl-containing samples were colourless immediately after PLAL experiments and turned yellow-green with time, reaching a light yellow-green colour after 24 h of shelf life at room temperature (21 °C). The gradual change in colloidal colour is a sign of the completion of the Cu NP reduction process. No particle sedimentation or agglomeration was observed in any of the HCl-containing samples immediately after PLAL,

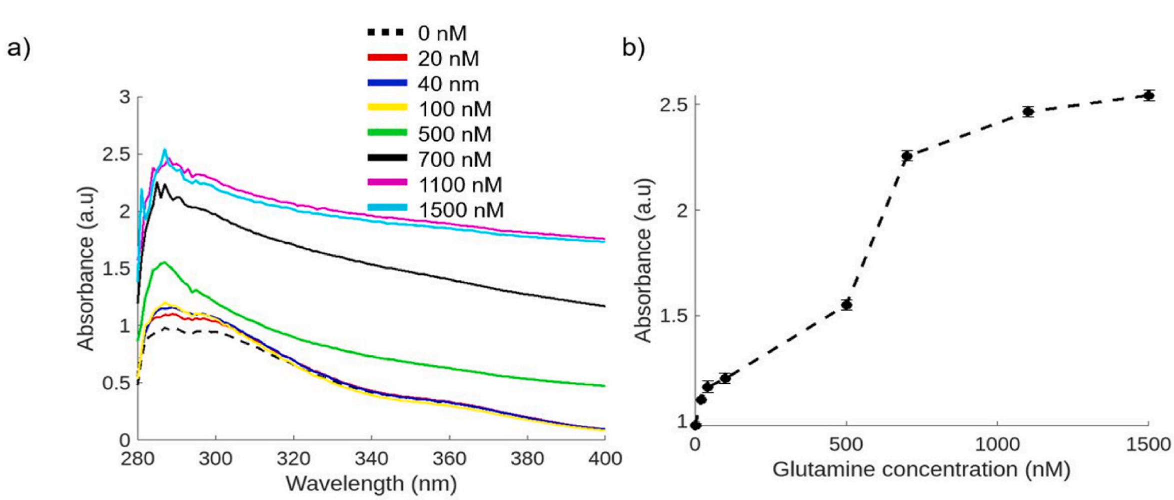

Fig. 6. a) Ultraviolet–visible spectroscopy analysis of $CuCl_2$ nanoparticles and glutamine; and b) correlation between glutamine concentration and absorbance, n = 3.

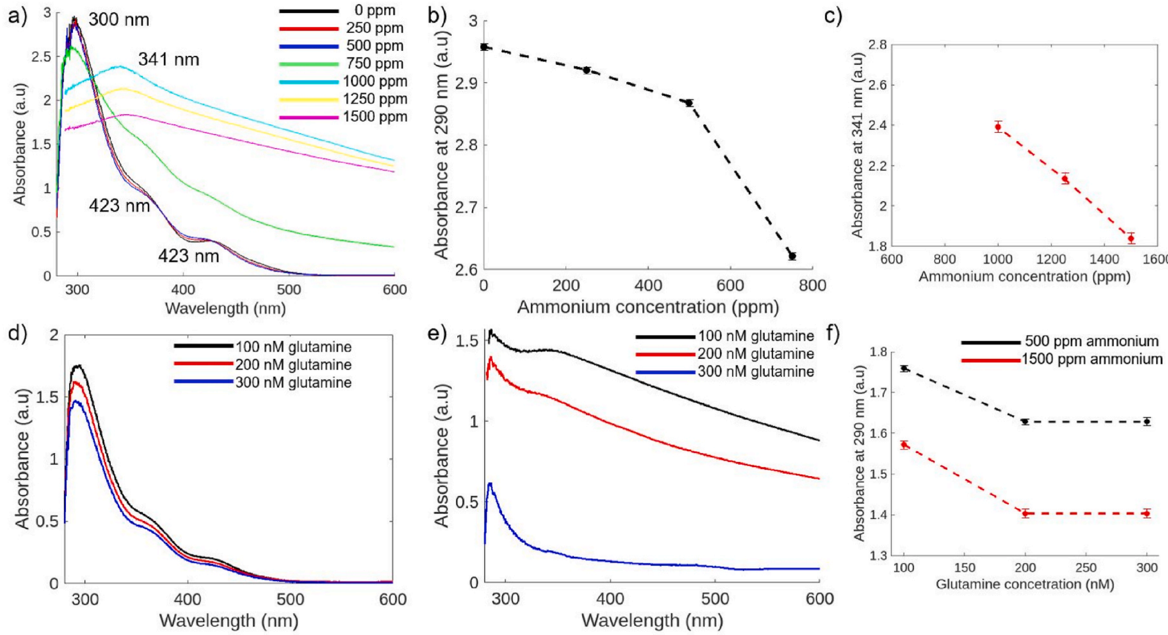

Fig. 7. a) Effect of ammonium concentration on the photoabsorption, b) effect of ammonia on photoabsorption at 300 nm, c) effect ammonia concentration on photoabsorption at 314 nm; and the effect of glutamine concentration on the absorbance in the presence of an ammonium concentration of d) 500 ppm, and e) 1500 ppm.

Table 1
Measured copper nanoparticle colloid properties.

Sample	Concentration (10^6 particles/ml)	Mean diameter (nm)	Relative ablation efficiency	Mean Zeta potential (mV)	Mean electrical conductivity (mS/cm)	Viscosity (mPa.s)
IPA-HCl (12 mM)	24.3	53	0.74	−32.1 ± 0.05	3.7 ± 0.1	3.2 ± 0.03
IPA-HCl (6 mM)	20.2	86	1	−42.7 ± 0.11	4.2 ± 0.2	3.5 ± 0.05
IPA	0.3	120	0.02	−0.9 ± 0.06	0.0005 ± 0.0003	2.1 ± 0.07

1hr after PLAL or 12 months after PLAL. Hence, the IPA-HCl hybrid liquid medium is demonstrated herein for the first time to be a stabilising agent for Cu NP production from PLAL.

Furthermore, Zeta potential measurements are the most common method of establishing colloidal stability. Colloids with Zeta potentials of magnitude <10 mV are considered neutral and unstable and the NPs are likely to aggregate and settle to the bottom. Colloids with Zeta potential magnitudes >30 mV are considered charged, stable and unlikely to exhibit particle aggregation due to the repulsive forces.

The $CuCl_2$ NPs exhibited a 47-fold larger Zeta potential magnitude (Table 1) than the CuO NPs and an 8400-fold larger electrical conductivity value (0.005 vs 4.2 mS/cm). The $CuCl_2$ NPs were also smaller than the CuO NPs (Table 1). Furthermore, a 50-fold higher ablation efficiency was recorded for $CuCl_2$ NPs than CuO NPs, which would translates to production cost savings. The $CuCl_2$ NPs are therefore a better candidate for conductive inks than the CuO NPs. The typical electrolyte conductivity of lithium-ion batteries is in the range of 0.05–10 mS/cm [44,45]. To that end, the Cu NP colloids fabricated herein also have the potential to be applied in nano-batteries owing to their high conductivities. The formation of $CuCl_2$ within the IPA-HCl liquid is attributed to the chlorine supplied by the liquid medium during NP formation. The atoms from the liquid medium are also vaporised along with the target during the PLAL process and are available for bonding during NP nucleation, growth and ageing [15,35,38]. In one study, PLAL was studied in the dichlorination of 1,4-Dichlorobenzene, where it broke down the liquid medium and released chlorine gas [34]. Gas chromatography measured chlorine removal, with a direct-pulsed laser process of 266 nm and 10 mJ/pulse power achieving 95% decomposition in just 15 min. Laser beam profile also affected removal efficiency, with a multipath laser irradiation system achieving more than 95% dechlorination efficiency in 5 min. Thus, the multipath system increased surface area exposed to the laser beam, speeding up the dechlorination reaction compared to a single pathway. This study and demonstrated that the liquid medium is heavily involved during the PLAL process. The formation mechanism of CuO NPs involves the bonding of oxygen atoms from liquid IPA with Cu atoms in the cavitation bubble during nucleation. The presence of oxygen during EDX analysis can also be attributed to the air and the oxygen attached to the NPs during drying prior to analysis. Research has shown that organic compounds reduce oxidation levels during PLAL compared to DI water due to their lower oxygen ratios [39,46]. In contrast to water, which has a 2:1 hydrogen to oxygen ratio, organic solvents have a much lower oxygen ratio and are dominated by carbon and hydrogen atoms.

Moreover, the NP shape is controlled by the rate of nucleation and growth, which is in turn controlled by various factors including temperature, pH, seeds and supersaturation. A review by Wu et al. [47] in 2016 explained some of the mechanisms that control the NP shape including adsorption growth, agglomeration, orientation attachment, underpotential deposition and Ostwald ripening. After the nucleus is formed during the initial stages of PLAL, the growth rate of the NPs increases with increasing surface free energy and the number of surface defects. A high surface free energy drives the nucleus to grow fast leading to the formation of spherical NPs rather than anisotropic ones. Furthermore, agglomeration, which is caused by Van Der Waal forces, the collision of NPs, high surface free energy and their small nanoscale size, tends to favour the formation of spherical, oval and quasi-spherical NPs such as the CuO NPs herein. Repulsive forces among NPs influence the NP growth direction, reduce NP agglomeration and were reported to be a suitable mechanism for producing anisotropic NPs such as the pyramidal-shaped ones in Fig. 2 [47]. Additionally, Liebig et al. [48] reported the formation of triangular Au NPs instead of spherical ones when a surfactant (dioctyl sodium sulfosuccinate) was used. The formation of triangular NPs was attributed to the diffusion-limited Ostwald ripening growth mechanism. The average growth rate of the NPs was 16 nm^3/min while the growth rate in the vertical direction was only 0.02 nm/min hence flat triangles were formed, similar to the $CuCl_2$ flat pyramidal NPs herein. The surfactant molecules attached to specific crystal faces and broke the symmetry (spherical shape). Within the aforementioned work, the Au NPs started as spheres and transformed into triangles with time. Herein, the time evolution of the NP shape was not studied in detail, however, Fig. 2c shows evidence of a few small spherical NPs among the pyramidal ones, which suggests that the pyramidal particles could have also started as spheres. The aforementioned is in agreement with previous findings in the literature which show that the NPs start as small spheres with a narrow size distribution within the plasma plume resulting from the thermodynamic equilibrium between the processes of nuclei growth and the evaporation [39].

$CuCl_2$ forms octahedral bond structures, while CuO forms cubic structures, which may contribute to the observed differences in final nanoparticle shapes. Our research team previously found that a concentration of HCl below 3 mM in the HCl-IPA liquid medium resulted in spherical nanoparticles instead of pyramidal ones [49]. This concentration corresponds to a pH of 1.9, while the 6 mM and 12 nM concentrations used in this study had similar pH values between 1.9 and 1.6, suggesting that the actual concentration of HCl affects NP shape but not pH value. However, pH has been shown to affect other PLAL process outputs, such as NP size and yield [39,50–54]. Despite this, few reports have investigated the influence of pH on the PLAL process, highlighting a gap in the literature that warrants further analysis.

The mean viscosity of pure IPA-HCl liquid was 1.3 mPa s while the Cu colloids had mean viscosities of 2.1 mPa s (IPA-synthesised sample), 3.2 mPa s (IPA-HCl-synthesised sample, 12 mM HCl) sample) and 3.5 mPa s (IPA-HCl-synthesised sample, 6 mM HCl). The Cu NPs increased the viscosity of IPA. The viscosity increased with increasing NP concentration and size as shown in Table 1. The viscosity of the as-fabricated colloids can be low for some conductive ink applications. For example, some inkjet printers require ink viscosities between 4 and 8 mPa s [55]. Glycerol was added to Cu colloids at different concentrations (1, 2, 5 and 10 %v/v) to increase the viscosity. The viscosity increased linearly with increasing glycerol concentration and values up to 5.2 mPa s were recorded at 10 %v/v glycerol.

4.2. Glutamine and ammonia detection application

Plasmon biochemical sensors have gained much attention in the literature owing to their fast response time, easy data accusation, high resolution, high repeatability and low mass [1,2,14]. Herein, the fabricated $CuCl_2$ NPs showed high UV–Vis absorbance and were assessed for biochemical sensing of glutamine. Glutamine is an amino acid whose concentration can be used as a biomarker for health conditions including neurologic disorders. Fig. 6b shows a recorded increase in absorbance of $CuCl_2$ NPs 300 nm with increasing glutamine concertation. A similar measurement technique was reported by Jiang et al. [14] who recorded a polynomial relationship between the H_2O_2 concentration and UV–Vis absorbance at 426 nm. Some recent plasmon sensors in the literature that employed similar detection mechanisms are displayed in Table 2.

Non-invasive methods of diagnosis such as the biochemical analysis of urine and sweat samples are more convenient methods than invasive methods owing to the lower cost, no pain to the patient is induced and a quicker analysis can be done. Ammonia is excreted through sweat and urine and its concentration is regulated therefore, deviations in normal concentrations are indicative of health issues. Urine from healthy humans is composed of about 96% water, 2% urea (includes ammonia and amino acids such as glutamine), 0.1% creatinine, and the rest comprises of salts such as potassium and phosphates [56]. The normal ammonium concentration in healthy human urine is below 10 ppm [20,21,57]. Measurements of ammonia concentration in urine can be used to diagonise urinary tract infection, hyperammonemic encephalopathy and hepatic disease [23,24].

In one study, ammonia levels greater than 14 ppm (79.5 μmol/l) from human urine samples were associated with a higher probability of

Table 2
Plasmon sensors based on nanoparticles.

Method of synthesis	NP composition	Detection mechanism	Detected molecule	Ref
Cu NPs were synthesised from Cu powder ablated via an Nd:YAG pulsed laser under IPA-HCl liquid	$CuCl_2$	UV–Vis absorbance of the 300 nm plasmon peak increased with increasing glutamine concentration	Glutamine (0.2–1500 nM)	herein
ZnO NPs were synthesised via a hydrothermal method	ZnO	Colloidal potential difference (mV) increased with increasing glutamine concentration	Glutamine (100–10 000 nM)	[2]
Au NPs were synthesised by the reduction of $HAuCl_4$ using H_2SO_4	Au	Colloidal potential difference (mV) increased with increasing glutamine concentration	Glutamine (100–800 nM)	[13]
Ag–Au NPs were sythesised by the reduction of $HAuCl_4$ and $AgNO_3$ ions by E.coli extracts	Ag–Au bimetallic	UV–Vis absorbance at the 426 nm plasmon peak increased with increasing H_2O_2 concentration	H_2O_2 (16–250 μM)	[14]
Au–MnO were synthesised by reduction of Mn ions in the presence of Au NPs followed by annealing	Au–MnO bimetallic	Current through a glassy carbon electrode increased with increasing H_2O_2 concentration	H_2O_2 (8–100 nM)	[19]
WO_3 NPs were synthesised via flame spray pyrolysis followed by doping with Cr to stabilise the ε phase	Cr-WO_3	A decrease in electrical resistance was caused by an increase in acetone concentration	Acetone (3–17 μM)	[58]
Ag NPs were synthesised via the reduction of $AgNO_3$ by sodium and functionalised with glutamine and histidine	Ag-glutamine-histidine	UV–Vis red-shift of the 407 nm plasmon peak to 480 nm and a sharp colour change from yellow to orange with increasing Hg^{2+} ion concentration	Hg^{2+} ions (1–500 μM)	[17]
Au NPs were synthesised by reducing $HAuCl_4$ in the presence of lead perchlorate, mercuric acetate, sodium hydroxide and polyvinylpyrrolidone	Au	UV–Vis red-shift of the 570 nm shift with increasing ion concentration	Hg^{2+} and Pb^{+} ions (0.1–1 μM)	[18]
Au NPs were synthesised by reducing $HAuCl_4$ in the presence of Mercury perchloride and cadmium perchloride and were fictionalised by papain	Au-Papain	UV–Vis absorbance ratio of the 626 and 524 nm plasmon peaks depended on the type of ion present	Hg^{2+}, Pb^{2+} and Cu^{2+} ions (1–40 μM)	[59]
Ag NPs synthesised by the reduction of $AgNO_3$ using fresh neem leaf extracts	Ag	Changes in UV–Vis absorbance and red and blue shifts of the 411 nm plasmon peak depending on the type of ion	Hg^{2+} and Pb^{2+} ions (20–200 μM)	[60]
Ag NPs synthesised from a $AgNO_3$ solution by a precipitation method	Ag	Changes in UV–Vis absorbance of the 428 nm peak was correlated to changes in ammonia concentration	Ammonia (10,000–60,000 ppm)	[1]
Cu NPs synthesised via a one-pot method from a $CuSO_4{\cdot}5H_2O$ solution	Cu	Changes in UV–Vis absorbance at 652 nm is proportional to H_2O_2 concentrations	Glucose and H_2O_2 (0.001–1mM)	[3]

liver and kidney failures [21]. Certain ammonia concentrations in urine are also indicative of diabetes [20]. Hence, urine and sweat ammonia concentrations are used for health monitoring and non-invasive diagnosis.

The $CuCl_2$ NPs could measure both glutamine concentration (Fig. 6) and ammonia concentration (Fig. 7 a-c) independently. It was recorded that a visible and immediate colour change occurs at certain ammonia concentrations (≥750 ppm), which can be used for quick qualitative measurements. In real-life situations, the urine/sweat ammonia could interfere with the glutamine readings given that the $CuCl_2$ NPs can interact with both. Therefore, the sensor should be able to detect glutamine concentrations in the presence of ammonia. The ammonia concentration in urine is less than 10 ppm. An increase in the $CuCl_2$ colloid from 0.5 μl to 1 μl increased the maximum absorbance from 1 to 3 a. u. At 3 a. u absorbance, low concentrations of ammonia (<250 ppm) could not change the absorbance statistically significantly hence, glutamine concentrations can be accurately measured independently of fluctuations in ammonia concentrations under 250 ppm. This solves the interference issue in urine samples.

An increase in ammonia concentration above 250 ppm causes interference with glutamine measurements as shown in Fig. 7d and e. In the absence of ammonia, an increase in glutamine concentration caused an increase in UV–Vis absorbance. Conversely, in the presence of ammonia (>250 ppm), an increase in glutamine concentration caused a decrease in UV–Vis absorbance. Fig. 7d and e shows glutamine readings in the presence of ammonia concentrations of 500 ppm and 1500 ppm respectively. The glutamine concentration now has an inversely proportional relationship with the absorbance, which is the opposite of what it was at ammonium concentrations below 250 ppm. Additionally, the absorbance values depend on the amount of ammonia present. In both cases (500 and 1500 ppm ammonia), the absorbance is inversely proportional to the glutamine concentration. The resilience of the sensor in the presence of other molecules such as potassium and phosphates requires investigation. More experimental data, coupled with machine learning algorithms could be used to increase the accuracy and stability of the plasmon sensor. This in trun could lead to a breakthrough in non-invasive, cheap, high resolution, accurate and high throughput detection and monitoring of glutamine concentrations.

4.3. Optical properties

Ultraviolet–visible spectroscopy gives information about the optical properties of the NPs; particularly it gives information about how much light at a certain wavelength is absorbed by the particles. Each material exhibits district peaks on the UV–Vis spectrum and these can be used to identify the material. Either CuO NPs or $CuCl_2$ NPs were synthesised depending on the liquid medium according to the EDX and XPS analysis. The liquid medium is involved during all stages of the ablation process; from electron cloud formation [15], through plasma plume formation, cavitation bubble events, embryo formation, NP nucleation, NP growth and NP ageing [39]. Optical absorbing properties of the CuO and $CuCl_2$ are shown in Fig. 5 a and b respectively. The differences in plasmon peak absorbance and wavelength are attributed to differences in chemical composition. The $CuCl_2$ NPs displayed much better optical absorption properties than the CuO as evidenced by the much higher absorbance of over 20-fold (factoring in dilution factors).

The UV–Vis peak at 300 nm is attributed to either Cu metal or CuO while the peak around 600 nm is ascribed to Cu_2O [61–63]. It is worth mentioning that the 600 nm peak is the more oxidized version of Cu NPs while the 300 nm peak represents less oxidation. The peak at around 300 nm was previously attributed to the interband transition of copper electrons from a deep level of the valence band while the peak at around 600 nm is due to the interband transition of a copper electron from an upper level of the valence band known as the surface plasmon resonance peak [64,65]. Peaks at 363 and 423 nm instead of 600 nm were recorded for the IPA-HCl synthesised colloids is a clear sign of NP surface modification attributed to the H^+ and Cl^- ions. The peak at 363 has been previously attributed to the surface plasmon resonance of Cu NPs [66]. It is desirable in plasmon sensors for the Cu NPs to have multiple absorbance peaks thereby enabling them to be used over multiple wavelengths [26]. It has been reported that particle agglomeration reduces the UV–Vis absorbance of a colloid [65], which contributed to the lower absorbance values of the IPA sample. Given the specific absorption range and intensity of absorption that are pre-definable with the $CuCl_2$ NPs, the development of a UV light-detection sensor is an interesting application area.

Ammonia concentrations greater than 750 ppm induced a red-shift of the 300 nm Peak to 341 nm, a disappearance of the 363 and 423 nm peaks (as shown in Fig. 7) and a colloidal colour change from yellow-green to milky-white. Cu reacts with ammonia and ammonium ions to form the copper–ammonia complex ion ($[Cu(NH_3)_4]^{2+}$) [67,68]. As the concentration of the $[Cu(NH_3)_4]^{2+}$ ions reach a certain threshold, the optical properties of the colloid change drastically hence the red shift.

The FTIR spectra of dried Cu NPs that were synthesised in IPA are shown in Fig. 5d. A similar spectrum was published in 2019 by another research team who examined the properties of Cu NPs in biomedicine [61]. The peaks in the fingerprinting region between 500 and 700 cm^{-1} are attributed to oxygen-metal vibration. The existence of copper oxide is confirmed by the 566 and 628 cm^{-1} peaks which are ascribed to the bending vibrations of Cu_2–O [61,69] and Cu–O [61,70] respectively. The peaks in the functional group region around 3361 and 3196 cm^{-1} were previously attributed to the hydroxyl functional group stretching mode. Furthermore, the peaks in the functional group region around 1418 and 1645 cm^{-1} are attributed to sp^2 carbon groups and carbonyl groups respectively [61,70]. The carbon peaks are most likely coming from the carbon within the liquid IPA that has attached to the Cu NPs. FTIR reviewed the existence of CuO and Cu_2O for IPA synthesised samples which are in agreement with the UV–Vis data.

4.4. Future work

The plasmon sensor ($CuCl_2$ colloid) developed herein showed promise for the detection of glutaminein the presence of ammonia. The sensor is not linear and it exhibited UV–Vis red shift at certain concentrations. Therefore, more experiments are required which will explore various combinations of concentrations to improve the accuracy. Additionally, the $CuCl_2$ colloids exhibit a high conductivity. A correlation between changes in conductivity with changes in glutamine/ammonia concentration can be another detection mechanism. Potentially, the two mechanisms (photometric and conductometric) would be used in conjunction to increase sensing reliability. Cu reacts with ammonia and ammonium ions to form the copper–ammonia complex ion ($[Cu(NH_3)_4]^{2+}$) [49]. These are positively charged ions and they increase the Zeta potential of the colloid positive values from being previously negative (−42.7 mV). This can be used as yet another detection mechanism. The sensor will also be subjected to glutamine detection tests in the presence of potential interferences such as potassium ions and changes in temperature and pH. Machine learning algorithms have gained much attention in the literature owing to their ability to quickly learn trends without the need to deeply analyse the underpinning phenomenon. This enables for faster development of the sensor that was introduced for the first time herein. Cu NPs are highly reactive, making them a good candidate for the detection of multiple types of molecules, even in trace amounts. Glucose sensors are one of the most reported types of sensors owing to the rising cases of diabetes [3]. Future work can explore the detection of glucose using the same plasmon sensor and in the presence of other molecules. Additionally, the plasmon sensor can be applied in drinking water treatment for the detection and monitoring of ammonia [1].

$CuCl_2$ NPs have not been investigated as much as CuO NPs in literature and both version have their own merits and deserve more research for various applications. Another study confirmed that CuO NPs have markedly higher cytotoxicity than $CuCl_2$ NPs in human lung cell lines [71]. It also revealed that the impact of CuO NP varies depending on the dose, with even non-cytotoxic concentrations resulting in alterations in gene expression. Conversely, alterations in gene expression caused by $CuCl_2$ were only evident at toxic concentrations, which interfere with copper homeostasis. CuO NPs are by far more popular than $CuCl_2$ NPs in the literature. Cu NPs synthesised via PLAL are popular for their antibacterial properties which has been explored very well in the literature.

5. Conclusion

- The shape and chemical composition of Cu NPs were controlled using liquid media. Quasi-spherical CuO NPs were synthesised in IPA, while pyramidal metallic Cu and $CuCl_2$ NPs were synthesised in an IPA-HCl liquid medium.
- The plasmon property of the laser-synthesised $CuCl_2$ nanoparticles was utilized for the detection of changes in glutamine concentration in the presence of ammonia in the range of 20–1500 nM, with a limit of detection of 20 nM. This demonstrates potential applications of the sensor in non-invasive diagnosis and monitoring, such as the analysis of urine and sweat samples.
- An increase in glutamine concentration resulted in an increase in UV–Vis absorbance at 300 nm in the absence of ammonia, while in the presence of ammonia (>250 ppm), an increase in glutamine concentration caused a decrease in UV–Vis absorbance.
- The $CuCl_2$ NPs exhibited higher colloidal electrical conductivity compared to CuO NPs, with the highest conductivity recorded being 4.2 ± 0.2 mS/cm, which is comparable to the conductivity values of commercial battery electrolytes.

Author statement

Anesu Nyabadza: Conceptualization; Methodology; Software; Validation; Formal analysis; Investigation; Writing – original draft; Writing – original draft; Visualization; **Éanna McCarthy**: Conceptualization; Methodology; Software; Validation; Formal analysis; Investigation; Writing – original draft; Writing – original draft; Visualization: **Karsten Fleischer**: Conceptualization; Methodology; Software; Validation; Formal analysis; Investigation; Writing – original draft; Writing – original draft; Visualization; **Sithara Sreenilayam**: Writing – review & editing; Formal analysis; **Ahmed Al-Hamaoy**: Writing – review & editing; Validation; **Mercedes Vazquez**: Supervision; Resources; **Dermot Brabazon**: Resources; Writing – original draft, Supervision; Supervision; Funding acquisition; Writing – review & editing.

Declaration of competing interest

The authors declare that they have no known competing financial interests or personal relationships that could have appeared to influence the work reported in this paper.

Data availability

No data was used for the research described in the article.

Acknowledgement

This work is supported in part by a research grant from Science Foundation Ireland (SFI) under Grant Numbers 16/1571 RC/3872 and 19/US-C2C/3579; and is co-funded under the European Regional Development Fund and by I-Form industry partners.Spectroscopy and microscopy measurements were carried out at the Nano Research Facility (NRF) in Dublin City University, which was funded under the Programme for Research in Third Level Institutions (PRTLI) Cycle 5. The PRTLI is co-funded through the European Regional Development Fund (ERDF), part of the European Union Structural Funds Programme 2011–2015. The authors of this work also acknowledge the technicians at NRF for their assistance including Dr Barry O'Connell, Leah Nolan, Stephen Fuller and Dr Úna Prendergast.

Appendix A. Supplementary data

Supplementary data to this article can be found online at https://doi.org/10.1016/j.solidstatesciences.2023.107171.

References

[1] O.A. Abdelaziz, R.M. Abdallah, R.A. Khater, A.S. Abo Dena, I.M. El-Sherbiny, Optical ammonia-sensing probe based on surface-plasmon resonance of silver-nanoparticle-decorated superparamagnetic dendritic nanoparticles, Plasmonics 1 (2022) 1–12, https://doi.org/10.1007/S11468-022-01745-1/TABLES/1.
[2] D. Albayrak, E. Karakuş, A Novel Glutamine Biosensor Based on Zinc Oxide Nanorod and Glutaminase Enzyme from Hypocria Jecorina, 2014, pp. 92–97, https://doi.org/10.3109/21691401.2014.913055.
[3] L. Hu, Y. Yuan, L. Zhang, J. Zhao, S. Majeed, G. Xu, Copper nanoclusters as peroxidase mimetics and their applications to H2O2 and glucose detection, Anal. Chim. Acta 762 (2013) 83–86, https://doi.org/10.1016/J.ACA.2012.11.056.
[4] A. Nyabadza, M. Vázquez, S. Coyle, B. Fitzpatrick, D. Brabazon, Review of materials and fabrication methods for flexible nano and micro-scale physical property sensors, Appl. Sci. 11 (2021), https://doi.org/10.3390/app11188563, 1–36.
[5] V. Cruzat, M.M. Rogero, K.N. Keane, R. Curi, P. Newsholme, Glutamine: metabolism and immune function, supplementation and clinical translation, Nutrients 10 (2018) 1–31, https://doi.org/10.3390/nu10111564.
[6] A. Nyabadza, C. Shan, R. Murphy, M. Vazquez, D. Brabazon, Laser-synthesised magnesium nanoparticles for amino acid and enzyme immobilisation, Open 11 (2023), 100133, https://doi.org/10.1016/J.ONANO.2023.100133.
[7] M. Gleeson, Dosing and efficacy of glutamine supplementation in human exercise and sport training, J. Nutr. 138 (2008), https://doi.org/10.1093/JN/138.10.2045S.
[8] L.-P. Zhao, S.-Y. Chen, R.-R. Zheng, R.-J. Kong, X.-N. Rao, A.-L. Chen, H. Cheng, D.-W. Zhang, S.-Y. Li, X.-Y. Yu, L.-P. Zhao, R.-R. Zheng, X.-N. Rao, A.-L. Chen, S.-Y. Li, X.-Y. Yu, S.-Y. Chen, D.-W. Zhang, R.-J. Kong, H. Cheng, Self-delivery nanomedicine for glutamine-starvation enhanced photodynamic tumor therapy, Adv Healthc Mater 11 (2022), 2102038, https://doi.org/10.1002/ADHM.202102038.
[9] L. Lang, F. Wang, Z. Ding, X. Zhao, R. Loveless, J. Xie, C. Shay, P. Qiu, Y. Ke, N. F. Saba, Y. Teng, Blockade of glutamine-dependent cell survival augments antitumor efficacy of CPI-613 in head and neck cancer, J. Exp. Clin. Cancer Res. 40 (2021) 1–14, https://doi.org/10.1186/S13046-021-02207-Y/FIGURES/6.
[10] A. Nyabadza, M. Vázquez, D. Brabazon, Magnesium nanoparticle synthesis from powders via LASIS - effects of liquid medium, laser pulse width and ageing on nanoparticle size, concentration, stability and electrical properties, Colloids Surf. A Physicochem. Eng. Asp. (2022), 129651, https://doi.org/10.1016/J.COLSURFA.2022.129651.
[11] A. Nyabadza, M. Vázquez, B. Fitzpatrick, D. Brabazon, Effect of liquid medium and laser processing parameters on the fabrication of carbon nanoparticles via pulsed laser ablation in liquid towards paper electronics, Colloids Surf. A Physicochem. Eng. Asp. 636 (2022), 128151, https://doi.org/10.1016/J.COLSURFA.2021.128151.
[12] A. Nyabadza, M. Vázquez, S. Coyle, B. Fitzpatrick, D. Brabazon, Magnesium nanoparticle synthesis from powders via pulsed laser ablation in liquid for nanocolloid production, Appl. Sci. 11 (2021), 10974, https://doi.org/10.3390/APP112210974, 11 (2021) 10974.
[13] E. Zeynaloo, Y.P. Yang, E. Dikici, R. Landgraf, L.G. Bachas, S. Daunert, Design of a mediator-free, non-enzymatic electrochemical biosensor for glutamate detection, Nanomedicine 31 (2021), 102305, https://doi.org/10.1016/J.NANO.2020.102305.
[14] X. Jiang, X. Fan, W. Xu, R. Zhang, G. Wu, Biosynthesis of bimetallic Au-Ag nanoparticles using Escherichia coli and its biomedical applications, ACS Biomater. Sci. Eng. 6 (2020) 680–689, https://doi.org/10.1021/ACSBIOMATERIALS.9B01297/SUPPL_FILE/AB9B01297_SI_001.PDF.
[15] A. Nyabadza, M. Vázquez, D. Brabazon, Modelling of Pulsed Laser Ablation in Liquid via Monte Carlo Techniques: the Effect of Laser Parameters and Liquid Medium on the Electron Cloud, Solid State Sci, 2022, 107003, https://doi.org/10.1016/J.SOLIDSTATESCIENCES.2022.107003.
[16] A. Nyabadza, J. Kane, S. Sreenilayam, M. Vázquez, D. Brabazon, S. Sreenilayam, D. Brabazon, Multi-material production of 4D shape memory polymer composites, in: Materials Science and Materials Engineering, Elsevier, 2021, pp. 879–894, https://doi.org/10.1016/B978-0-12-819724-0.00057-4. Elsevier, 2021.
[17] P. Buduru, B.C.S.R. Reddy, N.V.S. Naidu, Functionalization of silver nanoparticles with glutamine and histidine for simple and selective detection of Hg2+ ion in water samples, Sensor. Actuator. B Chem. 244 (2017) 972–982, https://doi.org/10.1016/J.SNB.2017.01.041.
[18] P. Nalawade, S. Kapoor, Gold nanoflowers based colorimetric detection of Hg2+ and Pb 2+ ions, Spectrochim. Acta Mol. Biomol. Spectrosc. 116 (2013) 132–135, https://doi.org/10.1016/J.SAA.2013.07.019.
[19] H. Zhu, A. Sigdel, S. Zhang, D. Su, Z. Xi, Q. Li, S. Sun, Core/shell Au/MnO nanoparticles prepared through controlled oxidation of AuMn as an electrocatalyst

for sensitive H2O2 detection, Angew Chem. Int. Ed. Engl. 53 (2014) 12508–12512, https://doi.org/10.1002/ANIE.201406281.
[20] A. Yudhana, S. Mukhopadhyay, O.D.A. Prima, S.A. Akbar, F. Nuraisyah, I. Mufandi, K.H. Fauzi, N.A. Nasyah, Multi sensor application-based for measuring the quality of human urine on first-void urine, Sens Biosensing Res 34 (2021), 100461, https://doi.org/10.1016/J.SBSR.2021.100461.
[21] M.F. Shalimar, R.P. Sheikh, B. Mookerjee, S.K. Agarwal, Acharya R. Jalan, Prognostic role of ammonia in patients with cirrhosis, Hepatology 70 (2019) 982–994, https://doi.org/10.1002/HEP.30534.
[22] T. Kenzaka, K. Kato, A. Kitao, K. Kosami, K. Minami, S. Yahata, M. Fukui, M. Okayama, Hyperammonemia in urinary tract infections, PLoS One 10 (2015), https://doi.org/10.1371/JOURNAL.PONE.0136220.
[23] C. Cordano, E. Traverso, V. Calabrò, C. Borzone, S. Stara, R. Marchese, L. Marinelli, Recurring hyperammonemic encephalopathy induced by bacteria usually not producing urease, BMC Res. Notes 7 (2014) 1–3, https://doi.org/10.1186/1756-0500-7-324/FIGURES/1.
[24] L. Zhao, J.H. Walline, Y. Gao, X. Lu, S. Yu, Z. Ge, H. Zhu, Y. Li, Prognostic role of ammonia in critical care patients without known hepatic disease, Front. Med. 7 (2020) 719, https://doi.org/10.3389/FMED.2020.589825/BIBTEX.
[25] M.F. Al-Hakkani, Biogenic copper nanoparticles and their applications: a review, SN Appl. Sci. 2 (2020) 1–20, https://doi.org/10.1007/s42452-020-2279-1.
[26] F. Parveen, B. Sannakki, M.v. Mandke, H.M. Pathan, Copper nanoparticles: synthesis methods and its light harvesting performance, Sol. Energy Mater. Sol. Cell. 144 (2016) 371–382, https://doi.org/10.1016/j.solmat.2015.08.033.
[27] V. Abhinav K, V.K. Rao R, P.S. Karthik, S.P. Singh, Copper conductive inks: synthesis and utilization in flexible electronics, RSC Adv. 5 (2015) 63985–64030, https://doi.org/10.1039/C5RA08205F.
[28] H. Siddiqui, M.R. Parra, P. Pandey, M.S. Qureshi, F.Z. Haque, Utility of copper oxide nanoparticles (CuO-NPs) as efficient electron donor material in bulk-heterojunction solar cells with enhanced power conversion efficiency, J. Sci.: Advanced Materials and Devices 5 (2020) 104–110, https://doi.org/10.1016/J.JSAMD.2020.01.004.
[29] P. Shen, Y. Liu, Y. Long, L. Shen, B. Kang, High-Performance polymer solar cells enabled by copper nanoparticles-induced plasmon resonance enhancement, J. Phys. Chem. C 120 (2016) 8900–8906, https://doi.org/10.1021/ACS.JPCC.6B02802/ASSET/IMAGES/LARGE/JP-2016-02802H_0008.JPEG.
[30] G. Di, M.R. Dabera, M. Walker, A.M. Sanchez, H.J. Pereira, R. Beanland, R. A. Hatton, Retarding oxidation of copper nanoparticles without electrical isolation and the size dependence of work function, 2017, Nat. Commun. 8 (2017) 1–8, https://doi.org/10.1038/s41467-017-01735-6, 1–10.
[31] É. McCarthy, S.P. Sreenilayam, O. Ronan, H. Ayub, R. McCann, L. McKeon, K. Fleischer, V. Nicolosi, D. Brabazon, Silver nanocolloid generation using dynamic Laser Ablation Synthesis in Solution system and drop-casting, Nano-Structures and Nano-Objects 29 (2022), 100841, https://doi.org/10.1016/j.nanoso.2022.100841.
[32] S.P. Sreenilayam, É. McCarthy, L. McKeon, O. Ronan, R. McCann, K. Fleischer, B. Freeland, V. Nicolosi, D. Brabazon, Additive-free silver nanoparticle ink development using flow-based Laser Ablation Synthesis in Solution and Aerosol Jet printing, Chem. Eng. J. 449 (2022), 137817, https://doi.org/10.1016/J.CEJ.2022.137817.
[33] S. Naik Shreyanka, J. Theerthagiri, S.J. Lee, Y. Yu, M.Y. Choi, Multiscale design of 3D metal–organic frameworks (M−BTC, M: Cu, Co, Ni) via PLAL enabling bifunctional electrocatalysts for robust overall water splitting, Chem. Eng. J. 446 (2022), 137045, https://doi.org/10.1016/J.CEJ.2022.137045.
[34] Y. Yu, A. Min, H.J. Jung, J. Theerthagiri, S.J. Lee, K.Y. Kwon, M.Y. Choi, Method development and mechanistic study on direct pulsed laser irradiation process for highly effective dechlorination of persistent organic pollutants, Environ. Pollut. 291 (2021), 118158, https://doi.org/10.1016/J.ENVPOL.2021.118158.
[35] J. Theerthagiri, K. Karuppasamy, A. Min, Unraveling the fundamentals of pulsed laser-assisted synthesis of nanomaterials in liquids: applications in energy and the environment COLLECTIONS ARTICLES YOU MAY BE INTERESTED IN, Appl. Phys. Rev. 9 (2022), 41314, https://doi.org/10.1063/5.0104740.
[36] J. Theerthagiri, S.J. Lee, K. Karuppasamy, J. Park, Y. Yu, M.L.A. Kumari, S. Chandrasekaran, H.S. Kim, M.Y. Choi, Fabrication strategies and surface tuning of hierarchical gold nanostructures for electrochemical detection and removal of toxic pollutants, J. Hazard Mater. 420 (2021), 126648, https://doi.org/10.1016/J.JHAZMAT.2021.126648.
[37] Y. Yu, S.J. Lee, J. Theerthagiri, S. Fonseca, L.M.C. Pinto, G. Maia, M.Y. Choi, Reconciling of experimental and theoretical insights on the electroactive behavior of C/Ni nanoparticles with AuPt alloys for hydrogen evolution efficiency and Non-enzymatic sensor, Chem. Eng. J. 435 (2022), 134790, https://doi.org/10.1016/J.CEJ.2022.134790.
[38] A. Nyabadza, M. Vazquez, D. Brabazon, A review of bimetallic and monometallic nanoparticle synthesis via laser ablation in liquid, Crystals 13 (2023) 253, https://doi.org/10.3390/CRYST13020253, 13 (2023) 253.
[39] E. Fazio, B. Gökce, A. De Giacomo, M. Meneghetti, G. Compagnini, M. Tommasini, F. Waag, A. Lucotti, C.G. Zanchi, P.M. Ossi, M. Dell'aglio, L. D'urso, M. Condorelli, V. Scardaci, F. Biscaglia, L. Litti, M. Gobbo, G. Gallo, M. Santoro, S. Trusso, F. Neri, Nanoparticles engineering by pulsed laser ablation in liquids: concepts and applications, Nanomaterials 10 (2020) 1–50, https://doi.org/10.3390/nano10112317.
[40] P. Wagener, S. Ibrahimkutty, A. Menzel, A. Plech, S. Barcikowski, Dynamics of silver nanoparticle formation and agglomeration inside the cavitation bubble after pulsed laser ablation in liquid, This Journal Is c the Owner Societies 15 (2013) 3068, https://doi.org/10.1039/c2cp42592k.
[41] D. Zhang, B. Gökce, S. Barcikowski, Laser synthesis and processing of colloids: fundamentals and applications, Chem. Rev. 117 (2017) 3990–4103, https://doi.org/10.1021/acs.chemrev.6b00468.
[42] Y. Pei, L. Wang, L. Huang, Generation of hydrogen under laser irradiation of organic liquids You may also like ISOBAM-stabilized Ni 2+ colloidal catalysts: high catalytic activities for hydrogen generation from hydrolysis of, KBH 4 (2018), https://doi.org/10.1070/QEL16648.
[43] C.K. Wu, M. Yin, S. O'Brien, J.T. Koberstein, Quantitative analysis of copper oxide nanoparticle composition and structure by X-ray photoelectron spectroscopy, Chem. Mater. 18 (2006) 6054–6058, https://doi.org/10.1021/cm061596d.
[44] E. Quartarone, P. Mustarelli, Review—emerging trends in the design of electrolytes for lithium and post-lithium batteries, J. Electrochem. Soc. 167 (2020), 050508, https://doi.org/10.1149/1945-7111/AB63C4.
[45] B. Boz, T. Dev, A. Salvadori, J.L. Schaefer, Review—electrolyte and electrode designs for enhanced ion transport properties to enable high performance lithium batteries, J. Electrochem. Soc. 168 (2021), 090501, https://doi.org/10.1149/1945-7111/ac1cc3.
[46] C.G. Moura, R.S.F. Pereira, M. Andritschky, A.L.B. Lopes, J.P. de F. Grilo, R.M. do Nascimento, F.S. Silva, Effects of laser fluence and liquid media on preparation of small Ag nanoparticles by laser ablation in liquid, Opt Laser. Technol. 97 (2017) 20–28, https://doi.org/10.1016/j.optlastec.2017.06.007.
[47] Z. Wu, S. Yang, W. Wu, Shape control of inorganic nanoparticles from solution, Nanoscale 8 (2016) 1237–1259, https://doi.org/10.1039/C5NR07681A.
[48] F. Liebig, A.F. Thu, J. Koetz, Ostwald Ripening Growth Mechanism of Gold Nanotriangles in Vesicular Template Phases, 2016, https://doi.org/10.1021/acs.langmuir.6b02662.
[49] A. Nyabadza, D. Brabazon, Bimetallic BaTiO3 and Cu nanoparticle synthesis via pulsed laser ablation in liquid of powder targets, Results in Engineering 17 (2023), 100994, https://doi.org/10.1016/j.rineng.2023.100994.
[50] Z. Yan, D.B. Chrisey, Pulsed laser ablation in liquid for micro-/nanostructure generation, J. Photochem. Photobiol. C Photochem. Rev. 13 (2012) 204–223, https://doi.org/10.1016/j.jphotochemrev.2012.04.004.
[51] F. Liebig, A.F. Thu, J. Koetz, A.F. Thünemann, J. Koetz, Ostwald ripening growth mechanism of gold nanotriangles in vesicular template phases, Langmuir 32 (2016) 10928–10935, https://doi.org/10.1021/acs.langmuir.6b02662.
[52] L. Li, K.Y. Mak, C.W. Leung, K.Y. Chan, W.K. Chan, W. Zhong, P.W.T. Pong, Effect of synthesis conditions on the properties of citric-acid coated iron oxide nanoparticles, Microelectron. Eng. 110 (2013) 329–334, https://doi.org/10.1016/J.MEE.2013.02.045.
[53] A. Baladi, R. Sarraf Mamoory, Investigation of different liquid media and ablation times on pulsed laser ablation synthesis of aluminum nanoparticles, Appl. Surf. Sci. 256 (2010) 7559–7564, https://doi.org/10.1016/J.APSUSC.2010.05.103.
[54] G. García Guillén, V.A. Zuñiga Ibarra, M.I. Mendivil Palma, B. Krishnan, D. Avellaneda Avellaneda, S. Shaji, Effects of liquid medium and ablation wavelength on the properties of cadmium sulfide nanoparticles formed by pulsed-laser ablation, ChemPhysChem 18 (2017) 1035–1046, https://doi.org/10.1002/cphc.201601056.
[55] S. Krainer, C. Smit, U. Hirn, The effect of viscosity and surface tension on inkjet printed picoliter dots, RSC Adv. 9 (2019) 31708–31719, https://doi.org/10.1039/C9RA04993B.
[56] N. Sarigul, F. Korkmaz, İ. Kurultak, A new artificial urine protocol to better imitate human urine, Sci. Rep. 9 (2019), https://doi.org/10.1038/S41598-019-56693-4.
[57] L. Liu, H. Mo, S. Wei, D. Raftery, Quantitative analysis of urea in human urine and serum by 1H nuclear magnetic resonance, Analyst 137 (2012) 595, https://doi.org/10.1039/C2AN15780B.
[58] L. Wang, A. Teleki, S.E. Pratsinis, P.I. Gouma, Ferroelectric WO3 nanoparticles for acetone selective detection, Chem. Mater. 20 (2008) 4794–4796, https://doi.org/10.1021/CM800761E/SUPPL_FILE/CM800761E-FILE002.PDF.
[59] Y. Guo, Z. Wang, W. Qu, H. Shao, X. Jiang, Colorimetric detection of mercury, lead and copper ions simultaneously using protein-functionalized gold nanoparticles, Biosens. Bioelectron. 26 (2011) 4064–4069, https://doi.org/10.1016/J.BIOS.2011.03.033.
[60] D. Karthiga, S.P. Anthony, Selective colorimetric sensing of toxic metal cations by green synthesized silver nanoparticles over a wide pH range, RSC Adv. 3 (2013) 16765–16774, https://doi.org/10.1039/C3RA42308E.
[61] S. Hemmati, S. Ahany Kamangar, A. Ahmeda, M.M. Zangeneh, A. Zangeneh, Application of copper nanoparticles containing natural compounds in the treatment of bacterial and fungal diseases, Appl. Organomet. Chem. 34 (2020) 1–16, https://doi.org/10.1002/aoc.5465.
[62] M. Fernández-Arias, M. Boutinguiza, J. del Val, C. Covarrubias, F. Bastias, L. Gómez, M. Maureira, F. Arias-González, A. Riveiro, J. Pou, Copper nanoparticles obtained by laser ablation in liquids as bactericidal agent for dental applications, Appl. Surf. Sci. 507 (2020), 145032, https://doi.org/10.1016/j.apsusc.2019.145032.
[63] A. Nag, L.M.F. Batista, K.M. Tibbetts, Synthesis of air-stable Cu nanoparticles using laser reduction in liquid, Nanomaterials 11 (2021), https://doi.org/10.3390/nano11030814.
[64] P. Gurav, S.S. Naik, K. Ansari, S. Srinath, K.A. Kishore, Y.P. Setty, S. Sonawane, Stable colloidal copper nanoparticles for a nanofluid: production and application, Colloids Surf. A Physicochem. Eng. Asp. 441 (2014) 589–597, https://doi.org/10.1016/j.colsurfa.2013.10.026.
[65] R.K. Swarnkar, S.C. Singh, R. Gopal, Effect of Aging on Copper Nanoparticles Synthesized by Pulsed Laser Ablation in Water: Structural and Optical Characterizations, 2011.
[66] M. Khatami, K. Ebrahimi, N. Galehdar, M.N. Moradi, A. Moayyedkazemi, Green synthesis and characterization of copper nanoparticles and their effects on liver

function and hematological parameters in mice, Turk J Pharm Sci 17 (2020) 412–416, https://doi.org/10.4274/TJPS.GALENOS.2019.28000.
[67] D. Guspita, A. Ulianas, Optimization of complex NH3 with Cu2+ ions to determine levels of ammonia by UV-Vis spectrophotometer, J Phys Conf Ser 1481 (2020), 012040, https://doi.org/10.1088/1742-6596/1481/1/012040.
[68] C. Peng, L. Chai, C. Tang, X. Min, Y. Song, C. Duan, C. Yu, Study on the mechanism of copper–ammonia complex decomposition in struvite formation process and enhanced ammonia and copper removal, J. Environ. Sci. 51 (2017) 222–233, https://doi.org/10.1016/J.JES.2016.06.020.
[69] R. Mukhopadhyay, J. Kazi, M.C. Debnath, Synthesis and characterization of copper nanoparticles stabilized with Quisqualis indica extract: evaluation of its cytotoxicity and apoptosis in B16F10 melanoma cells, Biomed. Pharmacother. 97 (2018) 1373–1385, https://doi.org/10.1016/J.BIOPHA.2017.10.167.
[70] T.B. Devi, M. Ahmaruzzaman, Facile preparation of Copper nanaoparticles using Coccinia grandis fruit extract and its application towards the reduction of toxic nitro compound, Mater. Today Proc. 5 (2018) 2098–2104, https://doi.org/10.1016/J.MATPR.2017.09.206.
[71] B.M. Strauch, R.K. Niemand, N.L. Winkelbeiner, A. Hartwig, Comparison between micro- and nanosized copper oxide and water soluble copper chloride: interrelationship between intracellular copper concentrations, oxidative stress and DNA damage response in human lung cells, Part. Fibre Toxicol. 14 (2017) 1–17, https://doi.org/10.1186/S12989-017-0209-1/FIGURES/10.